Exploring room-temperature microplasticity in a B2-strengthened refractory compositionally complex alloy

Aparajita Pramanik[a], Chethan Konkati[a], Stephan Laube[b], Liu Yang[b], Sandipan Sen[b], Alexander Kauffmann[b], Martin Heilmaier[b] and Ankur Chauhan[a*]

[a]Extreme Environments Materials Group (EEMG), Department of Materials Engineering, Indian Institute of Science (IISc), Bangalore, India, 560012

[b]Institute for Applied Materials (IAM-WK), Karlsruhe Institute of Technology (KIT), Engelbert-Arnold-Str. 4, 76131 Karlsruhe, Germany

[*]Corresponding author: ankurchauhan@iisc.ac.in

Abstract

The room-temperature microplasticity in a B2-precipitation-strengthened 27.3Ta–27.3Mo–27.3Ti–8Cr–10Al (at.%) body-centered cubic (BCC) refractory compositionally complex alloy (RCCA) was examined using nanoindentation under two aging conditions. Aging at 900 °C for 1 h resulted in nearly spherical B2 precipitates with a diameter of (5 ± 1) nm. Prolonged aging for 1000 h resulted in coarsened, elongated precipitates aligned along three orthogonal <001> directions, averaging (80 ± 16) nm in length, (26 ± 4) nm in width, and a volume fraction of 0.25 ± 0.05. Both conditions preserved a coherent precipitate-matrix interface with a small lattice parameter mismatch of + (0.6 ± 0.4) % after 1000 h, demonstrating good microstructural stability. Deformation at room temperature involved cooperative shearing of B2 precipitates by paired a/2⟨111⟩ dislocations, with an antiphase boundary energy of (167 ± 39) mJ/m². The dislocation-precipitate interaction transitioned from weakly-coupled pairwise cutting in the 1 h aged sample to strongly-coupled pairwise cutting in the 1000 h sample, causing a ~6–10% reduction in hardness. No Orowan looping, twinning, or phase transformation was observed.

Keywords: Refractory high entropy alloy; Nanoindentation; Plastic deformation; Precipitate-dislocation interactions; Anti-phase boundary energy

Graphical abstract

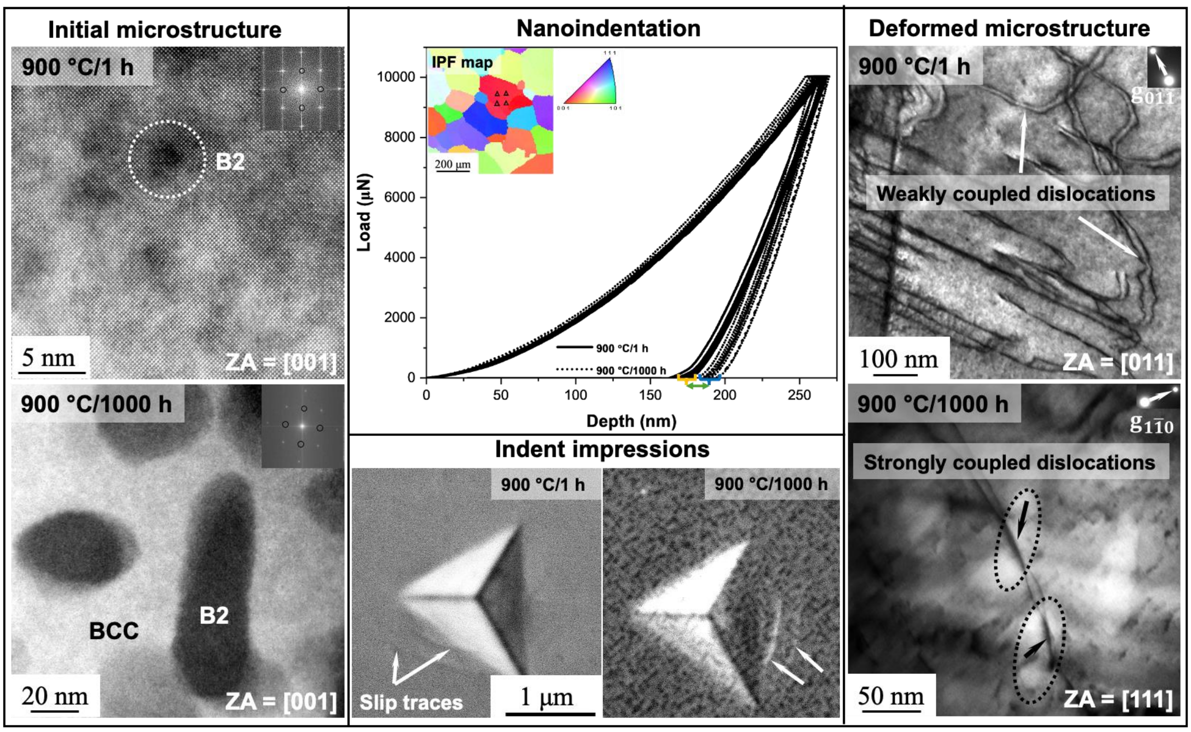

1. Introduction

Compositionally complex alloys (CCAs), introduced by Yeh et al. [1,2] and Cantor et al. [3] in the early 2000s, attracted significant attention for their exceptional mechanical properties at low temperatures. Building on this concept, Senkov et al. [4–7] developed refractory CCAs (RCCAs), which have shown great promise for high-temperature applications, potentially surpassing the operational limits of Ni-based superalloys [8,9]. Despite their potential, single-phase, solely solid solution-strengthened RCCAs exhibit limited creep resistance compared to state-of-the-art Ni-based superalloys [10,11]. This shortfall is attributed to the inherently faster diffusion rates in their open body-centered cubic (BCC) crystal structure and the absence of precipitation-strengthening [10].

To address these challenges, the current focus is on developing precipitate-strengthened RCCAs featuring B2-ordered precipitates within a BCC matrix analogous to the $L1_2$-strengthened Ni-based superalloys. These alloys aim to achieve creep resistances comparable to Ni-based counterparts by leveraging the strengthening effect of nanoscale precipitates [12–15]. In this context, low-density, oxidation-resistant alloys in the Ta–Mo–Ti–Cr–Al system have been recently designed to mimic a "superalloy-like" microstructure, with significant efforts directed toward evaluating their microstructural stability and mechanical properties [12,16–20].

One specific alloy composition, 27.3Ta–27.3Mo–27.3Ti–8Cr–10Al (at.%), exhibits a uniform distribution of B2-ordered precipitates embedded in a BCC matrix [12,19]. These precipitates form through a nucleation and growth process [19] with a solvus temperature (T_s) of approximately 1070 °C [16]. In polycrystalline condition, this alloy demonstrates exceptional creep resistance, comparable to the single-crystalline Ni-based superalloy CMSX-4, even at temperatures approaching the solvus temperature ($0.98T_s$) [16,19].

Although the microstructural evolution upon aging [19] and the creep response of this alloy have been recently reported [16], its deformation mechanisms, including precipitate-dislocation interactions at room and high temperatures, remain largely unexplored. Understanding this interaction is essential for evaluating alloy behavior [21], given the poor ductility of B2 intermetallics at ambient temperatures [22–24]. These insights can help to optimize aging treatments and guide RCCAs development.

Consequently, the present work aims to investigate the room-temperature deformation behavior of the 27.3Ta–27.3Mo–27.3Ti–8Cr–10Al (at.%) alloy in two exemplary aging conditions, with different precipitate size and morphology, using nanoindentation technique.

2. Experimental

2.1. Materials

The 27.3Ta–27.3Mo–27.3Ti–8Cr–10Al alloy was synthesized using high-purity metals (> 99.8 wt.% purity) through repetitive arc melting and casting in the Ar atmosphere. The cast button was then homogenized at 1600 °C for 20 h in the Ar atmosphere, followed by furnace cooling. The homogenized specimen was then wrapped in Mo foil, vacuum-sealed within a fused silica tube, and heat-treated at 1200 °C for 30 minutes, followed by water quenching. Subsequently, the as-quenched (AQ) specimens were rewrapped in Mo foil, vacuum-sealed in fused silica tubes, and subjected to aging heat treatments at 900 °C for 1 h and 1000 h, followed by water quenching.

2.2. Nanoindentation experiments

For nanoindentation, the aged specimens were sequentially polished using SiC papers up to P4000 grit, followed by 3 and 1 μm diamond suspensions, and finally polished with a 50 nm colloidal silica suspension for 16 hours using a Vibromet setup. Room-temperature nanoindentation tests were performed using a Triboindenter (Hysitron, Inc., Minneapolis, MN) equipped with a Berkovich diamond tip. Indents were placed entirely within <001>-oriented grains to avoid orientation-related variations and grain boundary contributions. The grains were identified using electron backscatter diffraction (EBSD) on a ThermoFisher Helios G4-UX SEM with an EDAX detector. The nanoindentation experiments employed a loading rate of 0.5 mN/s, a peak load of 10 mN, and a hold time of 10 seconds at the peak load. The average indentation depth is about 250 nm. A total of 25 indents were performed at each aging condition, maintaining a spacing of 10 μm between adjacent indents to avoid any overlap of plastic zones.

2.3. *Microstructural characterization*

Transmission electron microscope (TEM) samples were prepared in aged specimens and regions beneath indents using a ThermoFisher Scios-2 dual-beam focused-ion beam (FIB) system. Microstructural characterization was performed using scanning transmission electron microscopy (STEM) and conventional transmission electron microscopy (CTEM). Atomic-resolution imaging was conducted to analyze the precipitate-matrix interface using a probe-corrected ThermoFisher Titan Themis TEM at 300 kV, equipped with a high-angle annular dark-field (HAADF) detector in STEM mode. Diffraction contrast imaging was performed with a ThermoFisher Tecnai T20-ST TEM at 200 kV under parallel illumination.

3. Results and discussion

3.1. *Initial microstructure*

The HAADF-STEM micrographs in Fig. 1 showcase the evolution of precipitates in the 27.3Ta–27.3Mo–27.3Ti–8Cr–10Al alloy aged at 900 °C for two aging durations. After 1 h of aging (Fig. 1a), the microstructure features a high density of fine, nearly spherical precipitates with an average diameter of (5 ± 1) nm. Fig. 1b provides a high-magnification view, highlighting an individual dark-contrast precipitate embedded within the BCC matrix. In HAADF-STEM mode, image contrast primarily arises due to differences in atomic number (Z) [25]. Therefore, the dark contrast of the precipitates relative to the surrounding matrix indicates that they are enriched in lighter elements, while the matrix is more abundant in heavier elements. This observation agrees with recent findings on the same alloy [12,19], which showed that these precipitates are rich in Ti and Al, while the matrix contains higher concentrations of Ta and Mo, with Cr evenly distributed in both. The corresponding fast Fourier transform (FFT) in Fig. 1c shows superlattice spots (marked with dotted circles) indexed to the B2-ordered precipitates, while the unmarked fundamental diffraction spots correspond to both the BCC matrix and the B2 precipitates.

After aging for 1000 h, the precipitates have grown and coarsened as well as adopted an elongated morphology, extending in three orthogonal directions (horizontal, vertical, and in/out-of-plane), as shown in Fig. 1d and the high-magnification view in Fig. 1e. The FFT of this sample (Fig. 1f) closely resembles that of the 1 h aged sample (Fig. 1c), indicating a cube/cube orientation relationship between the precipitate and matrix with <100>B2 || <100>BCC and {110}B2 || {110}BCC, consistent across both aging conditions. Additionally, the elongated precipitates have grown along the <001> directions of the cubic lattice, aligning with the minimization of elastic strain energy [26], a phenomenon well documented for other BCC/B2 RCCAs [13,27]. These precipitates exhibit an average length of (80 ± 16) nm and a width of (26 ± 4) nm, contributing to a volume fraction of 0.25 ± 0.05. This aligns reasonably well with the data reported in [19], which recorded mean equivalent diameters of (35 ± 15) μm at volume fractions of (0.15 ± 0.03), despite limitations in probe size and the segmentation of scanning electron microscope (SEM) micrographs provided in Supplementary Material Section A.

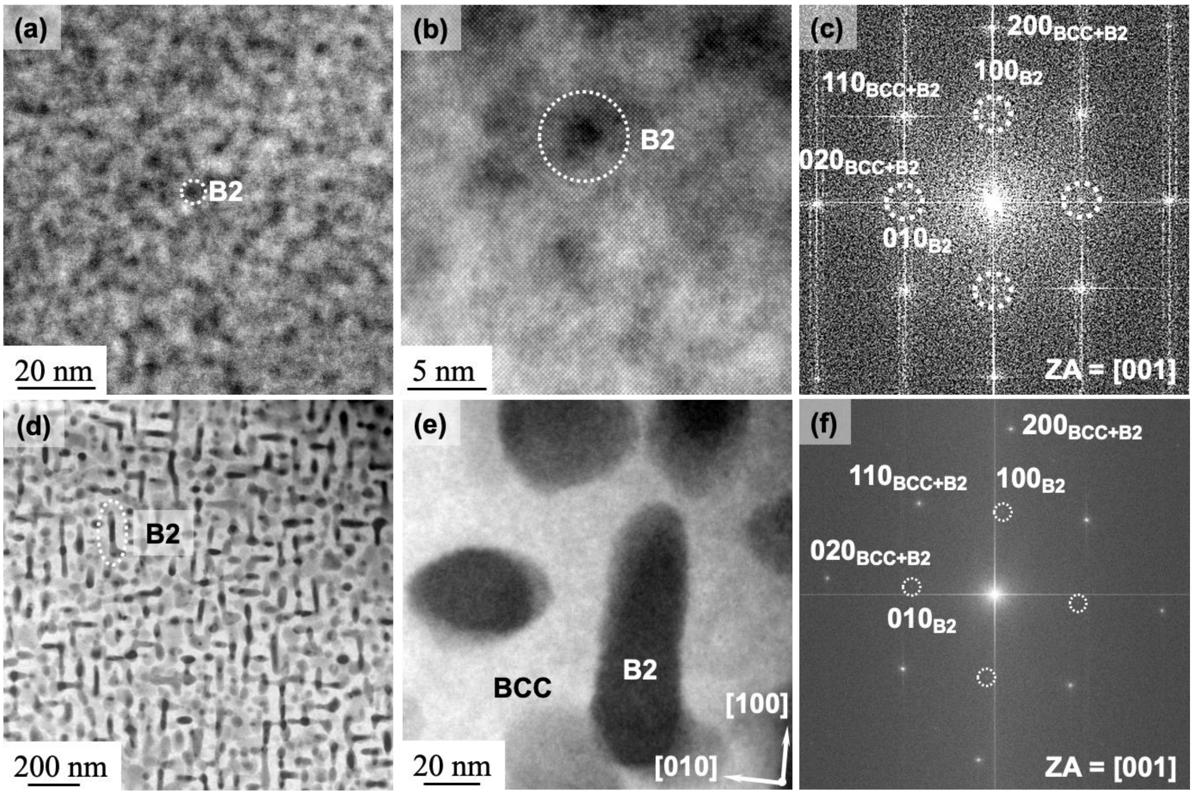

Fig. 1: HAADF-STEM micrographs from within the grains of the 27.3Ta–27.3Mo–27.3Ti–8Cr–10Al alloy aged at 900 °C for 1 h and 1000 h: (a) After 1 h of aging, microstructure showcases a high density of fine, dark-contrast, nearly spherical precipitates, magnified in (b). (c) The corresponding FFT shows superlattice spots (marked) from the B2 precipitates alongside unmarked diffraction spots common to both the BCC matrix and B2 precipitates. (d) After 1000 h of aging, the microstructure reveals coarsened, dark-contrast precipitates with an elongated morphology extending along three orthogonal directions (horizontal, vertical, and in/out-of-plane). (e) High-magnification micrograph from a region in (d). (f) The corresponding FFT closely resembles that of the 1 h aged sample, with elongated precipitates aligning along the <001> directions of the cubic lattice. ZA represents the zone axis.

To examine the interface characteristics between the BCC matrix and B2 precipitates in the two aging conditions, high-resolution (HR) STEM investigations were carried out. Fig. $2a_1$ shows an HR-STEM micrograph from the 1 h aged sample, illustrating a B2 precipitate within the BCC matrix, with the corresponding inverse FFT (IFFT) in Fig. $2a_2$ from the {110} diffraction spot in the FFT. Likewise, HR-STEM micrographs from the 1000 h aged sample in Fig. $2b_1$ and $2c_1$ and their IFFTs in Fig. $2b_2$ and $2c_2$, display the BCC/B2 interfaces at the rounded end and the lateral section of the elongated B2 precipitate. Evidently, the lattice fringes of the (110) atomic planes appear continuous across the precipitate-matrix interfaces in both aging conditions, confirming their coherent nature. However, in the 1000 h aged sample, lattice strain is observed around a few discontinuous (110) planes, particularly along the lateral surfaces of the elongated precipitates, indicating the presence of a few isolated dislocations (marked with symbol "⊥" in Fig. 2c₂).

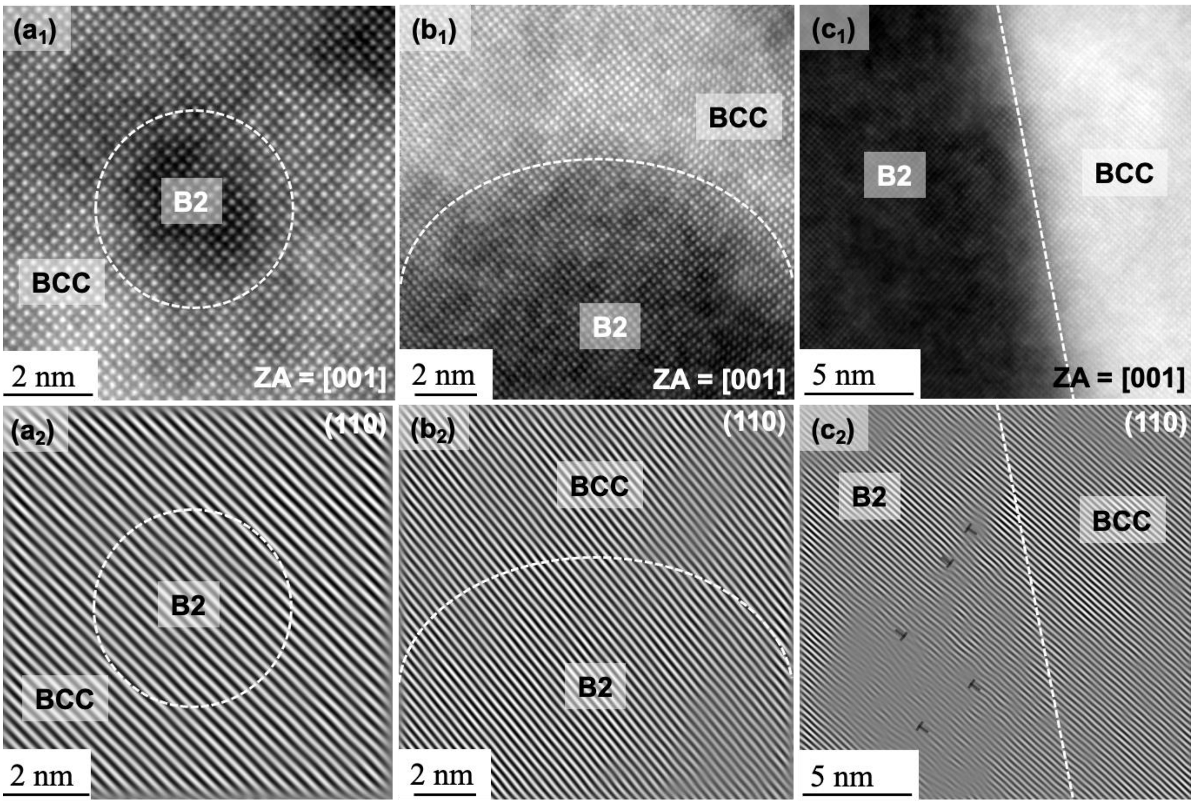

Fig. 2: (a$_1$) HR-STEM micrograph from the 1 h aged sample showing a B2 precipitate in the BCC matrix. (a$_2$) Corresponding IFFT from the {110} diffraction spot in the FFT of (a$_1$). (b$_1$) HR-STEM micrograph from the 1000 h aged sample showing the rounded end of an elongated B2 precipitate in the BCC matrix. (b$_2$) Corresponding IFFT derived from the {110} diffraction spot in the FFT of (b$_1$). (c$_1$) HR-STEM micrograph from the 1000 h aged sample, focusing on the lateral section of an elongated B2 precipitate in the BCC matrix. (c$_2$) Corresponding IFFT derived from the {110} diffraction spot in the FFT of (c$_1$), with occasional dislocations (⊥) observed along the interface. ZA represents the zone axis.

To estimate the difference in lattice parameters of the BCC/B2 phases in the 1000 h aged sample, lattice parameters were derived from the HR-STEM micrographs, measuring (0.323 ± 0.001) nm for the BCC matrix and (0.325 ± 0.001) nm for the B2 precipitates. Using these values, the relative lattice parameter mismatch, defined as $\delta = \frac{a_{\mathrm{B2}} - a_{\mathrm{BCC}}}{0.5(a_{\mathrm{B2}} + a_{\mathrm{BCC}})}$, where a_{B2} and a_{BCC} are the lattice parameters of the precipitate and matrix, respectively [28], was estimated to be + (0.6 ± 0.4) %. A low positive δ is consistent with the recently reported P-type rafting during creep of the present alloy at temperatures of 1000 °C and above [16]. Generally, determining the accurate δ using HR-STEM is challenging due to the uncertainties inherent in the highly localized nature of the investigations. Techniques such as X-ray diffraction [28], synchrotron X-rays, neutron diffraction [29], or convergent beam electron diffraction (CBED) in TEM [30,31] offer greater precision but, at present, are beyond the scope of this study. Nevertheless, the low δ confirms that the interface to be coherent despite a few isolated dislocations. It is important to note that the term "lattice parameter mismatch" is preferred over "misfit" in this context to emphasize that the results in our study are potentially influenced by elastic and plastic relaxation or constraints within the lattices. Misfit, as defined in various theoretical models, typically excludes such relaxation or constraint effects.

3.2. Nanoindentation response

Nanoindentation experiments were carried out to examine the room-temperature micro-plasticity in samples aged at 900 °C for 1 and 1000 h. Multiple indents were performed within <001>-oriented grains to ensure reproducibility (Fig. 3a), with representative indents for the two aged conditions shown in Fig. 3b and 3c. Slip traces near the indent, without any evidence of cracking, confirm a purely elastic-plastic response under both aged conditions. The load-depth curves in Fig. 3d exhibit minor differences between the two aging conditions, with the elastic-to-plastic transition region showcasing several pop-in events at nearly constant loads (see inset, Fig. 3d$_1$). Despite the variations, the curves obtained from the 1000 h-aged sample exhibit a slightly greater indentation depth than the 1 h-aged sample, indicating lower hardness. Using the Oliver-Pharr method [32], the obtained average hardness value is also slightly higher for the 1 h aged sample (9.0 ± 0.2 GPa) compared to the 1000 h aged sample (8.5 ± 0.3 GPa). A similar trend was observed in microhardness measurements reported in [19], with the 1 h aged sample showcasing a higher hardness of (7.2 ± 0.1) GPa compared to (6.5 ± 0.2) GPa for the 1000 h aged sample (see Supplementary Material Section A). The observed variation between the nanoindentation and microhardness values may likely stem from the indentation size effect, where hardness typically increases with decreasing indentation size [33]. Overall, the hardness decreased by approximately 6–10% after 1000 h of aging, likely due to the growth and coarsening of B2 precipitates.

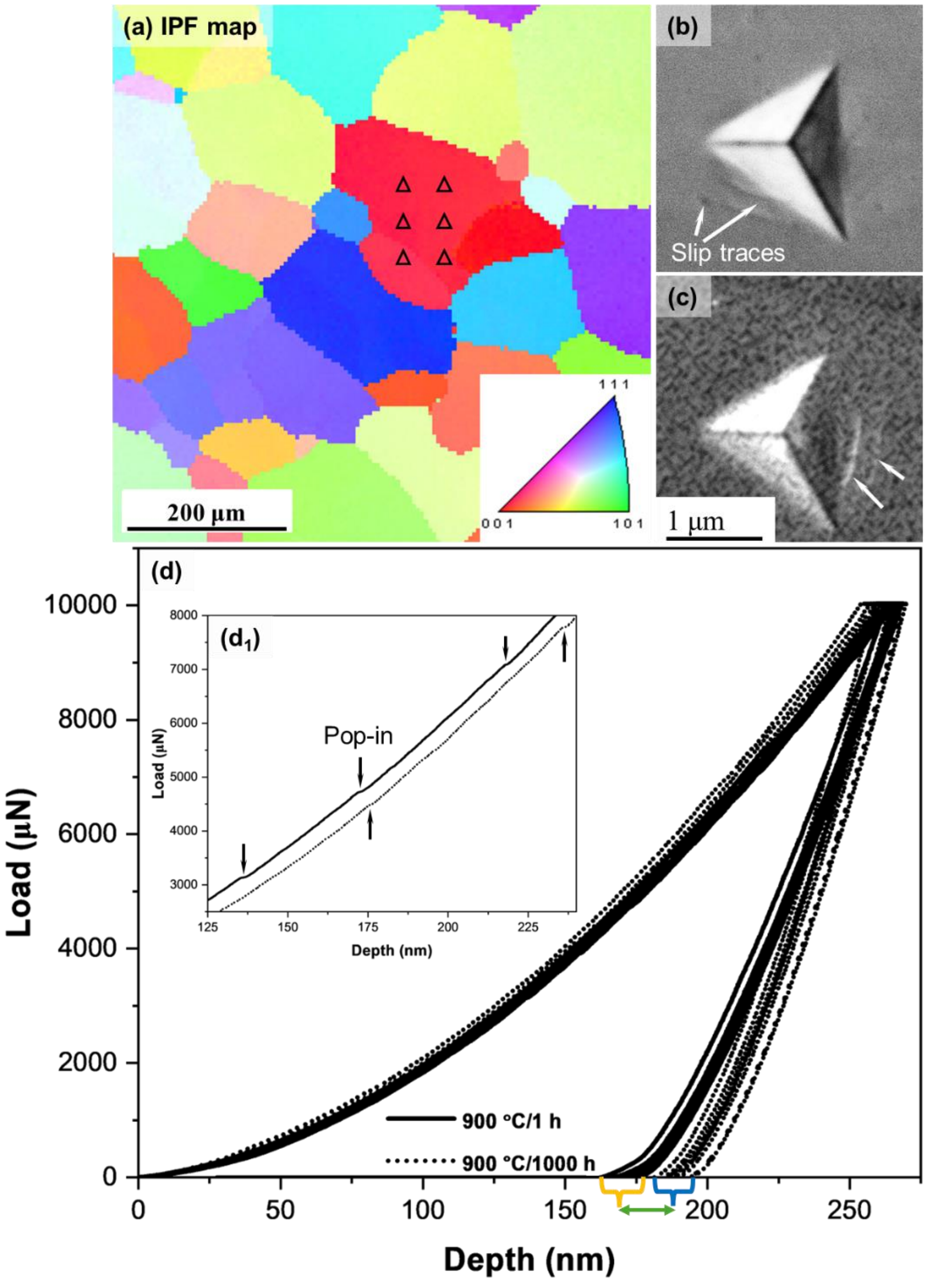

Fig. 3: Room-temperature nanoindentation response of the 27.3Ta–27.3Mo–27.3Ti–8Cr–10Al alloy under two aging conditions: (a) Schematic representation of indents within a <001>-oriented grain superimposed on an EBSD-derived inverse pole figure (IPF) map, with the corresponding color key shown in the lower-right inset, obtained from the 1000 h aged sample. (b, c) Secondary electron (SE)-SEM micrographs highlighting representative indents within grains of the (b) 1 h aged and (c) 1000 h aged samples. Slip traces near the indents, without any evidence of cracking, confirm a purely elastic-plastic response for both conditions. (d) Multiple load-depth curves from <001>-oriented grains show minor differences between the two aging conditions, with slightly deeper indentation depths observed in the 1000 h aged sample. (d_1) Magnified loading curves from each aging condition show pop-in events, indicated with arrows.

3.3. Deformation mechanisms

TEM lamellae were prepared from beneath the indents to correlate the active deformation mechanisms with the hardness response for the two aging conditions. Fig. 4a presents a bright field (BF)-TEM micrograph showcasing a deformed region beneath the indent in the 1 h aged sample. The crack-free plastic zone shows a high density of dislocations, while the surrounding undeformed area remains dislocation-free. Deformation features include slip bands (SBs) oriented in various directions, indicating the activation of multiple slip systems. The region outlined with a dashed square in Fig. 4a, showcasing distinct individual dislocations, was analyzed to determine their Burgers vector. Tilting the same area to different diffraction vectors (g) makes the dislocations invisible, enabling the identification of their Burgers vectors as ½$[11\bar{1}]$. The Supplementary Material Section B summarizes the g·b calculations supporting this determination.

Additionally, the magnified micrographs in Fig. 4b–d reveal that the 1 h aged sample primarily displays weakly coupled dislocations, characterized by widely spaced leading and trailing dislocations. The spacing was measured to be in the range of 8 to 20 nm, which is 1.6 to 4 times the average diameter of the B2 precipitates in the 1 h aged condition. Slip bands (SBs), highlighted with ellipses in Fig. 4b and 4d, further demonstrate arrays of weakly coupled dislocations, indicating a tendency for planar slip, likely facilitated by glide plane softening [34]. Occasionally, the leading dislocation appears bowed between the pinning points (likely B2 precipitates), while the trailing dislocation remains relatively straight, as shown within the dashed rectangle in Fig. 4c. Besides, the above-mentioned weakly coupled configurations, the 1 h aged sample occasionally also displayed relatively strongly coupled dislocations, with leading and trailing dislocations in close proximity (spacing less than 4 nm), as indicated by arrows in Fig. 4b and 4d.

The deformed region in the 1000 h aged sample also displays varying distances between dislocation pairs as they shear through and move between precipitates, reflecting distinct interaction mechanisms inside and outside the precipitates. BF-TEM micrographs (Fig. $5a_1$ and $5b_1$) and the corresponding weak-beam dark field (WBDF) micrographs (Fig. $5a_2$ and $5b_2$) reveal a more pronounced form of the strongly coupled dislocation configuration compared to the 1 h aged sample. Indicated by arrows, the leading and trailing dislocations here appear almost merged and have likely moved together within the precipitates.

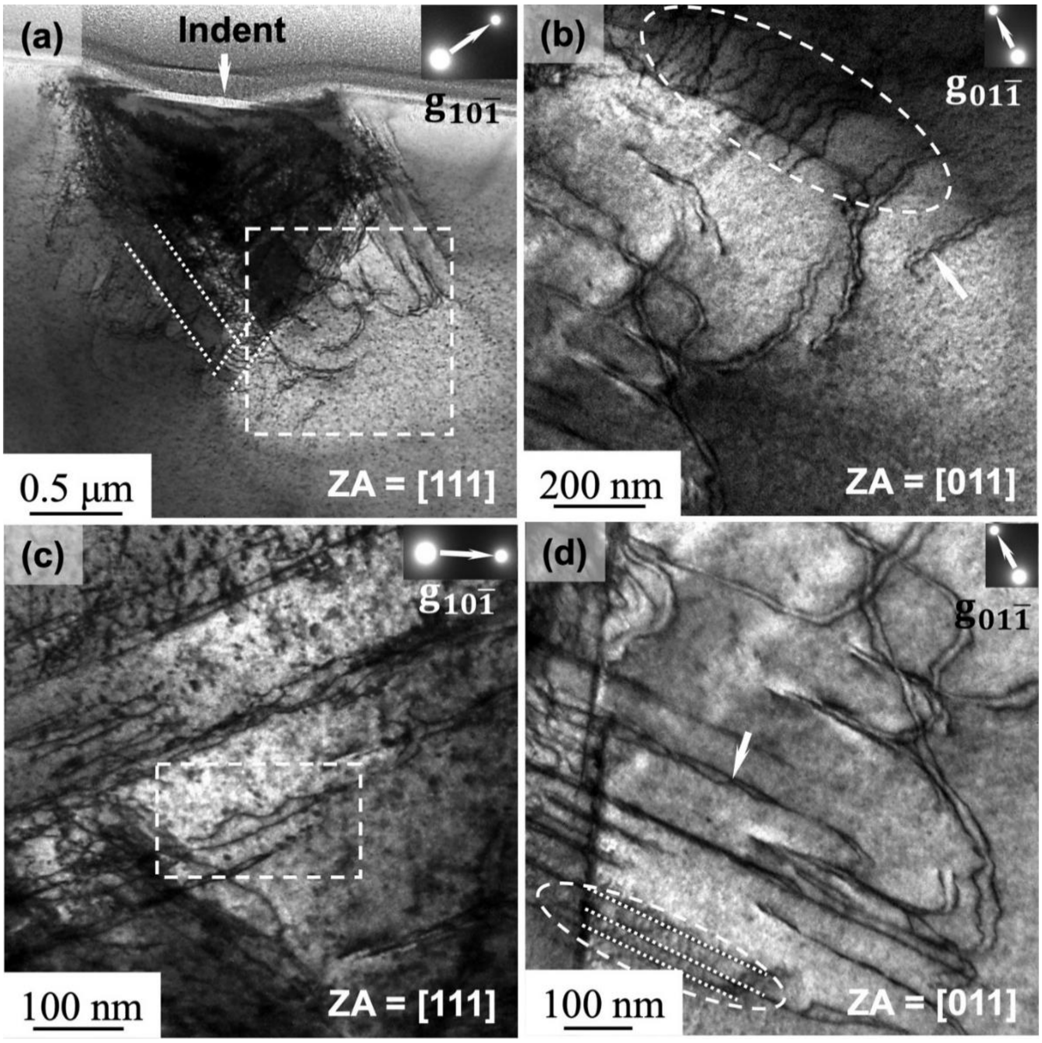

Fig. 4: BF-TEM micrographs revealing deformation characteristics beneath an indent in the 1 h aged sample. (a) The crack-free plastic zone has high dislocation density, while the surrounding area is dislocation-free. Slip bands (SBs) in various orientations indicate the activation of multiple slip systems. The square-marked area was analyzed to determine the Burgers vector of dislocations. (b–d) Magnified views reveal weakly coupled dislocations. The region marked in (c) shows a bowed leading dislocation, while the trailing dislocation is relatively straight. Arrows in (b) and (d) point to occasional strongly coupled dislocation configurations. ZA represents the zone axis.

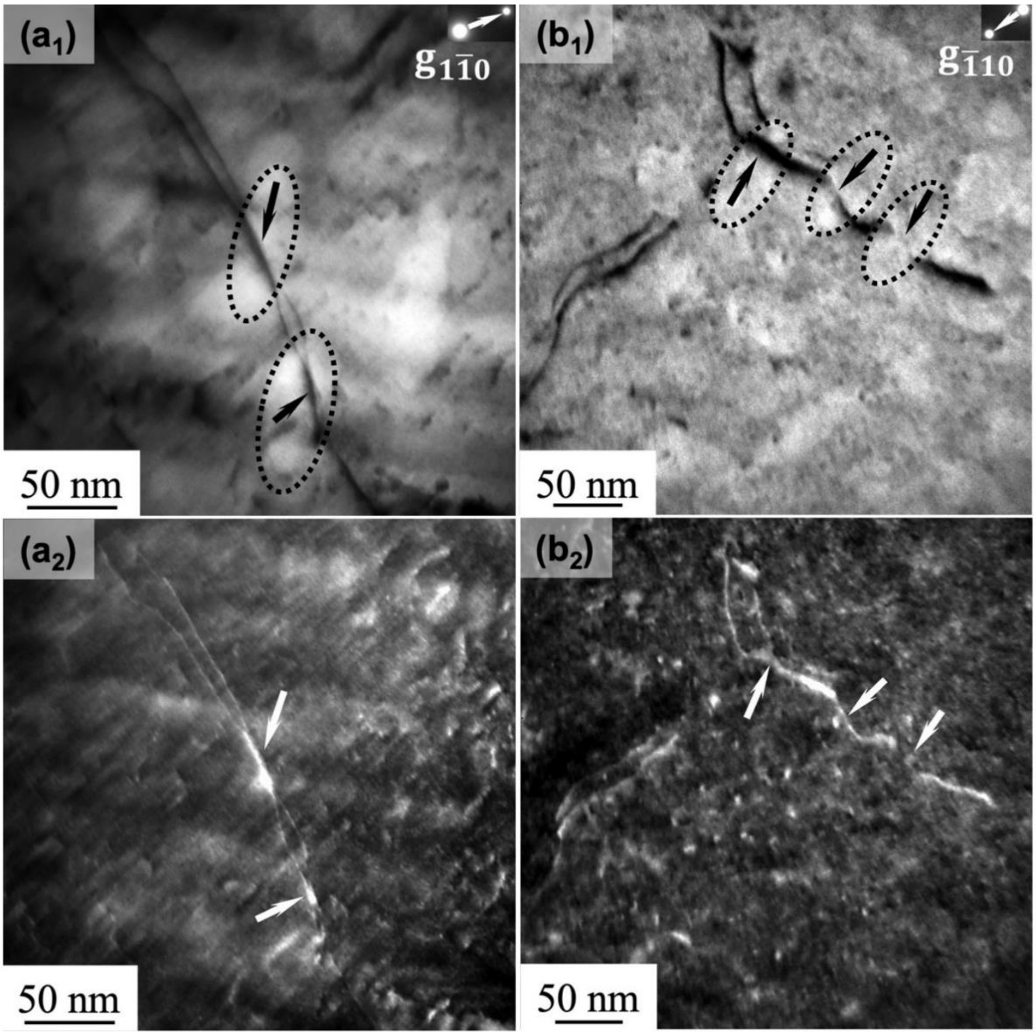

Fig. 5: BF-TEM micrographs (a$_1$) and (b$_1$), along with their corresponding WBDF micrographs (a$_2$) and (b$_2$), obtained beneath an indent in the 1000 h aged sample, show variations in dislocation pair spacing as they shear through or move between precipitates. Arrows indicate an intensified version of a strongly coupled dislocation configuration, where leading and trailing dislocations are nearly merged and move together. ZA represents the zone axis.

Overall, pairwise shearing of the B2 precipitates was observed under both aging conditions, with predominantly weakly coupled configurations in the 1 h aged sample, transitioning to strongly coupled configurations in the 1000 h aged sample. Similar dislocation configurations have been reported in γ'-strengthened Ni-based superalloys [35–38]and BCC HfMoNbTaRu RCCA with B2 precipitates [14]. However, as discussed later, no evidence of Orowan looping was observed. Additionally, twinning and phase transformation were not observed under either aging condition, consistent with findings reported for single-phase BCC HfNbTiZr high-entropy alloy [39]. It has been suggested that the presence of B2 precipitates inhibits the coordinated motion required for twinning and phase transformation [40]. Consequently, it can be stated that dislocations primarily mediate the nanoindentation pop-in events shown in Fig. 3d$_1$.

As previously discussed, the studied alloy features precipitates with an ordered B2 crystal structure embedded in a BCC matrix, the dislocation within the latter having a Burgers vector of $\frac{a}{2} < 111 >$ type. As commonly accepted, $\frac{a}{2} < 111 >$ is not a lattice translation vector in the B2 structure. When a typical $\frac{a}{2} < 1\bar{1}1 > \{110\}$ BCC matrix dislocation shears through a B2 precipitate; the disorder creates an internal antiphase boundary (APB) within the precipitate. To restore the internal order, dislocations pair up with a characteristic spacing, where the trailing $\frac{a}{2} < 1\bar{1}1 > \{110\}$ dislocation of the pair eliminates the APB created by the leading dislocation. This dislocation pairing is influenced by three forces: (1) The Peach-Koehler force generated by the applied stress, (2) A repulsive force between same-sign dislocations within the glide plane, and (3) Interaction with the APB in the precipitate, where the leading dislocation experiences a repulsive force (due to APB formation) and the trailing dislocation an attractive force (due to APB elimination) [41,42]. These interactions govern the dislocation behavior during the shearing of the precipitates and play a critical role in the alloy's deformation response.

The equilibrium spacing between dislocation pairs is affected by their position inside or outside the precipitate, with the spacing inside the precipitate being influenced by its size, volume fraction, and APB energy [41]. For constant volume fraction of precipitates and depending on the APB energy, the dislocation pair spacing decreases with increasing precipitate size. In the case of smaller precipitates, as observed for the 1 h aged sample (Fig. 4), the spacing often spans multiple precipitates [41–43], as illustrated schematically in Fig. 6a. This configuration is referred to as weakly or loosely coupled dislocations.

As precipitate size increases, weakly coupled dislocations gradually approach each other, eventually transitioning into a strongly coupled configuration. In this configuration, the dislocation pair becomes confined within a single precipitate, as occasionally observed in the 1 h aged sample (Fig. 4) and predominantly in the 1000 h aged sample (Fig. 5). For the elongated precipitates in the 1000 h aged sample, the dislocation pairs tend to interact with precipitates in regions of the highest local curvature (i.e., the smallest effective radius of the curvature [44]). This results in a more intensified version of a strongly coupled dislocation configuration. Here, the leading and trailing dislocations appear almost merged and move together within the precipitates, as a superdislocation with $a < 111 >$ type Burgers vector (Fig. $5a_1$ and $5b_1$), as shown schematically in Fig. 6b.

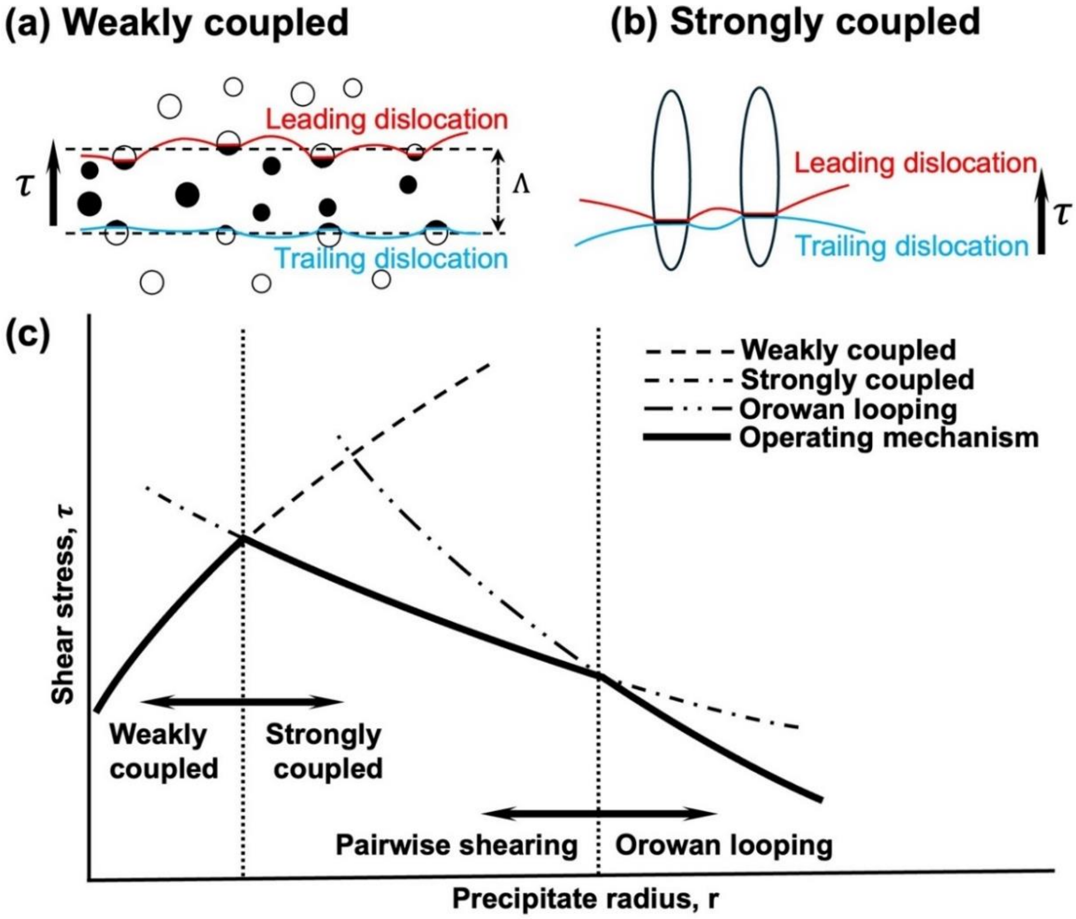

Fig. 6: (a) and (b) show weakly (adapted from [41]) and strongly coupled dislocation-precipitate configurations. Solid and hollow regions of the precipitate indicate areas with and without an APB. (c) A schematic shows the relative strength contributions of pairwise shearing and Orowan looping mechanisms [45] [44], with the operating mechanism marked with a bold line.

Fig. 6c schematically illustrates the strengthening contributions of pairwise shearing (weakly and strongly coupled cases) and Orowan looping mechanisms as a function of precipitate size for constant volume fraction. For weakly coupled dislocations, shear resistance scales approximately with the square root of the particle radius [44]. In contrast, for strongly coupled dislocations, it scales inversely with the square root of the particle radius [41,42]. Consequently, the curve in Fig. 6c displays a steep, positive slope in the weakly coupled regime, signifying a rapid strength increase with small changes in precipitate radius. In contrast, a gradual negative slope is seen in the strongly coupled regime, indicating a gradual decrease in strength despite large changes in the precipitate radius [37]. Peak strength occurs at the transition between the two regimes. Also, strong coupling between dislocation pairs reduces the APB formation rate, decreasing alloy strength [41]. This shift in dislocation-precipitate interaction, from predominantly weakly coupled pairwise cutting in the 1 h peak-aged sample to strongly coupled pairwise cutting in the 1000 h over-aged sample, decreases hardness.

3.4. APB energy estimation

Since APB energy is a key factor influencing the observed deformation mechanisms, estimating it is of significant interest. However, due to the small size of the precipitates and the influence of multiple forces on the dissociation width, direct observation and calculation of the APB dissociation width from TEM were not feasible. As a result, an alternative approach using microhardness value and established equations was employed for APB energy estimation. The average microhardness value of the 1 h aged specimen, as mentioned above, is approximately 7.2 GPa (also see Supplementary Material section A [19]), which corresponds to an estimated yield stress of around 2.4 GPa using Tabor's approach ($Yield\ stress \simeq \frac{Hardness}{3}$) [46]. The yield stress of the studied alloy has two primary contributing sources: solid solution strengthening and precipitation hardening. The solid solution strengthening contribution in the studied alloy can be approximated from the reported average microhardness value of the as-quenched (AQ) condition, which is approximately 5.7 GPa [19], resulting in a yield strength of about 1.9 GPa. By subtracting this solid solution contribution from the yield strength of the 1 h aged specimen, a precipitation hardening contribution of 500 MPa is obtained.

Converting normal stress to shear stress using the relation $\sigma = M\tau$ (with M = 3.067 [47]) gives a shear stress (τ) of approximately 160 MPa. Assuming that the precipitation hardening is primarily due to the order strengthening, and using the equation $\Delta\tau_{peak} = 0.56\left(\frac{\gamma}{b}\right)f^{1/2}$ [35] (where $\Delta\tau_{peak}$ is the maximum strength increment from order hardening, γ is the APB energy, b is the Burgers vector of the matrix, and f is the volume fraction of the precipitates), and with $\Delta\tau_{peak}$ of 160 MPa, b estimated as $\frac{a}{2} < 111 >$ (approximately 0.2797 nm), and f of 0.25 ± 0.05 (assuming the volume fraction for the 1 h aged sample is the same as that of the 1000 h aged sample), the APB energy is calculated to be 167 ± 39 mJ/m^2. The uncertainty in the APB value is estimated based on the upper and lower bounds of the peak hardness and precipitate volume fraction. This estimated APB value is comparable to that of B2 precipitates (176 mJ/m^2 at 500 °C) in the $Al_{10}Nb_{15}Ta_5Ti_{30}Zr_{40}$ alloy [48], higher than HfRu B2 precipitates (54 mJ/m^2) in as-cast equiatomic HfMoNbTaRu RCCA [14] and lower than traditional B2 compounds like NiAl (810 mJ/m^2) and FeAl (300 mJ/m^2) [49]. As noted earlier, no Orowan looping was observed under the present aging conditions, a phenomenon previously noted in B2-strengthened HfMoNbTaRu RCCA [14] and coarse NiAl precipitates in Al-Ni-Cr-Mo-Zr-B-Fe alloy [50]. This absence of Orowan looping can be attributed to the coherent, nano-sized B2 precipitates with relatively low APB energy in the present aged conditions. However, Orowan looping can occur as these precipitates grow (see Fig. 6e) and lose coherency with further aging, warranting further investigations. Finally, as peak strength is directly proportional to APB energy, alloying strategies should aim to optimize precipitate compositions with higher APB energy while maintaining low misfit to improve the strength of the alloy.

4. Conclusions

In summary, this study investigates the room-temperature deformation behavior of a B2-strengthened 27.3Ta–27.3Mo–27.3Ti–8Cr–10Al (at.%) RCCA, focusing on the effects of aging at 900 °C for 1 and 1000 h. The microstructure analysis revealed that 1 h aging resulted in nearly spherical B2 precipitates (~5 nm). In contrast, 1000 h aging led to coarsened, elongated precipitates aligned along three orthogonal <001> directions, with an average length of (80 ± 16) nm, width of (26 ± 4) nm, and a volume fraction of 0.25 ± 0.05. Both aging conditions maintained a coherent precipitate-matrix interface, with a minimal δ estimated to be + (0.6 ± 0.4) %, indicating stable microstructure at 900 °C. Deformation mechanisms involved cooperative shearing of B2 precipitates by paired a/2⟨111⟩ dislocations, with an antiphase boundary energy of (167 ± 39) mJ/m². The dislocation-precipitate interaction evolved from weakly coupled pairwise cutting in the 1 h-aged sample to strongly coupled pairwise cutting in the 1000 h-aged sample, leading to a 6–10% decrease in hardness. Neither Orowan looping nor twinning or phase transformation was observed under the investigated conditions.

Acknowledgments

AC gratefully acknowledges financial support from the Infosys Foundation, Bangalore. AP and AC acknowledge the Advanced Centre for Microscopy and Microanalysis (AFMM) and its staff at IISc, Bengaluru, for providing access to the characterization facilities. The financial support by the Deutsche Forschungsgemeinschaft (DFG), grant no. HE 1872/34-2 is also gratefully acknowledged. LY is financially supported by the China Scholarship Council (CSC) with No. 202207000023.

Data availability

Data will be made available on request.

References

[1] J. -W. Yeh, S. -K. Chen, S. -J. Lin, J. -Y. Gan, T. -S. Chin, T. -T. Shun, C. -H. Tsau, S. -Y. Chang, Nanostructured High-Entropy Alloys with Multiple Principal Elements: Novel Alloy Design Concepts and Outcomes, Adv. Eng. Mater. 6 (2004) 299–303. https://doi.org/10.1002/adem.200300567.

[2] J.-W. Yeh, S.-J. Lin, T.-S. Chin, J.-Y. Gan, S.-K. Chen, T.-T. Shun, C.-H. Tsau, S.-Y. Chou, Formation of simple crystal structures in Cu-Co-Ni-Cr-Al-Fe-Ti-V alloys with multiprincipal metallic elements, Metall. Mater. Trans. A 35 (2004) 2533–2536. https://doi.org/10.1007/s11661-006-0234-4.

[3] B. Cantor, I.T.H. Chang, P. Knight, A.J.B. Vincent, Microstructural development in equiatomic multicomponent alloys, Mater. Sci. Eng. A 375–377 (2004) 213–218. https://doi.org/10.1016/j.msea.2003.10.257.

[4] O.N. Senkov, G.B. Wilks, D.B. Miracle, C.P. Chuang, P.K. Liaw, Refractory high-entropy alloys, Intermetallics 18 (2010) 1758–1765. https://doi.org/10.1016/j.intermet.2010.05.014.

[5] O.N. Senkov, G.B. Wilks, J.M. Scott, D.B. Miracle, Mechanical properties of Nb25Mo25Ta25W25 and V20Nb20Mo20Ta20W20 refractory high entropy alloys, Intermetallics 19 (2011) 698–706. https://doi.org/10.1016/j.intermet.2011.01.004.

[6] O.N. Senkov, J.M. Scott, S.V. Senkova, D.B. Miracle, C.F. Woodward, Microstructure and room temperature properties of a high-entropy TaNbHfZrTi alloy, J. Alloys Compd. 509 (2011) 6043–6048. https://doi.org/10.1016/j.jallcom.2011.02.171.

[7] O.N. Senkov, J.M. Scott, S.V. Senkova, F. Meisenkothen, D.B. Miracle, C.F. Woodward, Microstructure and elevated temperature properties of a refractory TaNbHfZrTi alloy, J. Mater. Sci. 47 (2012) 4062–4074. https://doi.org/10.1007/s10853-012-6260-2.

[8] O.N. Senkov, S. Gorsse, D.B. Miracle, High temperature strength of refractory complex concentrated alloys, Acta Mater. 175 (2019) 394–405. https://doi.org/10.1016/j.actamat.2019.06.032.

[9] S. Gorsse, D.B. Miracle, O.N. Senkov, Mapping the world of complex concentrated alloys, Acta Mater. 135 (2017) 177–187. https://doi.org/10.1016/j.actamat.2017.06.027.

[10] C. Gadelmeier, Y. Yang, U. Glatzel, E.P. George, Creep strength of refractory high-entropy alloy TiZrHfNbTa and comparison with Ni-base superalloy CMSX-4, Cell Rep. Phys. Sci. 3 (2022) 100991. https://doi.org/10.1016/j.xcrp.2022.100991.

[11] C.-J. Liu, C. Gadelmeier, S.-L. Lu, J.-W. Yeh, H.-W. Yen, S. Gorsse, U. Glatzel, A.-C. Yeh, Tensile creep behavior of HfNbTaTiZr refractory high entropy alloy at elevated temperatures, Acta Mater. 237 (2022) 118188. https://doi.org/10.1016/j.actamat.2022.118188.

[12] S. Laube, S. Schellert, A. Srinivasan Tirunilai, D. Schliephake, B. Gorr, H.-J. Christ, A. Kauffmann, M. Heilmaier, Microstructure tailoring of Al-containing compositionally complex alloys by controlling the sequence of precipitation and ordering, Acta Mater. 218 (2021) 117217. https://doi.org/10.1016/j.actamat.2021.117217.

[13] J.-P. Couzinié, M. Heczko, V. Mazánová, O.N. Senkov, M. Ghazisaeidi, R. Banerjee, M.J. Mills, High-temperature deformation mechanisms in a BCC+B2 refractory complex concentrated alloy, Acta Mater. 233 (2022) 117995. https://doi.org/10.1016/j.actamat.2022.117995.

[14] C. Frey, H. You, S. Kube, G.H. Balbus, K. Mullin, S. Oppenheimer, C.S. Holgate, T.M. Pollock, High Temperature B2 Precipitation in Ru-Containing Refractory Multi-principal Element Alloys, Metall. Mater. Trans. A 55 (2024) 1739–1764. https://doi.org/10.1007/s11661-024-07368-x.

[15] C. Frey, B. Neuman, A. Botros, S.A. Kube, Tresa.M. Pollock, Refractory multi-principal element alloys with solution and aged HfRu-B2 precipitates, Scr. Mater. 255 (2025) 116411. https://doi.org/10.1016/j.scriptamat.2024.116411.

[16] L. Yang, S. Sen, D. Schliephake, R.J. Vikram, S. Laube, A. Pramanik, A. Chauhan, M. Heilmaier, A. Kauffmann, Creep behavior of a precipitation-strengthened A2-B2 refractory high entropy alloy, Karlsruher Institut für Technologie (KIT), 2024. https://doi.org/10.5445/IR/1000173956.

[17] H. Chen, A. Kauffmann, S. Seils, T. Boll, C.H. Liebscher, I. Harding, K.S. Kumar, D.V. Szabó, S. Schlabach, S. Kauffmann-Weiss, F. Müller, B. Gorr, H.-J. Christ, M. Heilmaier, Crystallographic ordering in a series of Al-containing refractory high entropy alloys Ta–Nb–Mo–Cr–Ti–Al, Acta Mater. 176 (2019) 123–133. https://doi.org/10.1016/j.actamat.2019.07.001.

[18] F. Müller, B. Gorr, H.-J. Christ, H. Chen, A. Kauffmann, S. Laube, M. Heilmaier, Formation of complex intermetallic phases in novel refractory high-entropy alloys NbMoCrTiAl and TaMoCrTiAl: Thermodynamic assessment and experimental validation, J. Alloys Compd. 842 (2020) 155726. https://doi.org/10.1016/j.jallcom.2020.155726.

[19] S. Laube, A. Kauffmann, S. Schellert, S. Seils, A.S. Tirunilai, C. Greiner, Y.M. Eggeler, B. Gorr, H.-J. Christ, M. Heilmaier, Formation and thermal stability of two-phase microstructures in Al-containing refractory compositionally complex alloys, Sci. Technol. Adv. Mater. 23 (2022) 692–706. https://doi.org/10.1080/14686996.2022.2132118.

[20] S. Laube, G. Winkens, A. Kauffmann, J. Li, C. Kirchlechner, M. Heilmaier, Strength of Disordered and Ordered Al-Containing Refractory High-Entropy Alloys, Adv. Eng. Mater. 26 (2024) 2301797. https://doi.org/10.1002/adem.202301797.

[21] S. Han, S. Laube, Z. Chen, A. Kauffmann, M. Heilmaier, H. Inui, Operative Slip System and Dislocation Behavior in a Brittle Refractory High-Entropy Alloy with the B2 Ordered Structure, (2024). https://doi.org/10.2139/ssrn.5037012.

[22] K. Ishida, R. Kainuma, N. Ueno, T. Nishizawa, Ductility enhancement in NiAl (B2)-base alloys by microstructural control, Metall. Trans. A 22 (1991) 441–446. https://doi.org/10.1007/BF02656811.

[23] R. Darolia, Ductility and fracture toughness issues related to implementation of NiAl for gas turbine applications, Intermetallics 8 (2000) 1321–1327. https://doi.org/10.1016/S0966-9795(00)00081-9.

[24] D.B. Miracle, M.-H. Tsai, O.N. Senkov, V. Soni, R. Banerjee, Refractory high entropy superalloys (RSAs), Scr. Mater. 187 (2020) 445–452. https://doi.org/10.1016/j.scriptamat.2020.06.048.

[25] D.B. Williams, C.B. Carter, eds., Transmission Electron Microscopy: A Textbook for Materials Science, 2nd ed., Springer US, Boston, MA, 2009. https://doi.org/10.1007/978-0-387-76501-3.

[26] M.E. Thompson, C.S. Su, P.W. Voorhees, The equilibrium shape of a misfitting precipitate, Acta Metall. Mater. 42 (1994) 2107–2122. https://doi.org/10.1016/0956-7151(94)90036-1.

[27] Z.T. Kloenne, J.-P. Couzinié, M. Heczko, R. Gröger, G.B. Viswanathan, W.A.T. Clark, H.L. Fraser, On the bcc/B2 interface structure in a refractory high entropy alloy, Scr. Mater. 223 (2023) 115071. https://doi.org/10.1016/j.scriptamat.2022.115071.

[28] H.-A. Kuhn, H. Biermann, T. Ungár, H. Mughrabi, An X-ray study of creep-deformation induced changes of the lattice mismatch in the γ'-hardened monocrystalline nickel-base superalloy SRR 99, Acta Metall. Mater. 39 (1991) 2783–2794. https://doi.org/10.1016/0956-7151(91)90095-I.

[29] U. Glatzel, Neutron scattering experiments with a nickel base superalloy part II: Analysis of intensity profiles, Scr. Metall. Mater. 31 (1994) 291–296. https://doi.org/10.1016/0956-716X(94)90285-2.

[30] R. Völkl, U. Glatzel, M. Feller-Kniepmeier, Measurement of the lattice misfit in the single crystal nickel based superalloys CMSX-4, SRR99 and SC16 by convergent beam electron diffraction, Acta Mater. 46 (1998) 4395–4404. https://doi.org/10.1016/S1359-6454(98)00085-8.

[31] B. Von Grossmann, H. Biermann, U. Tetzlaff, F. Pyczak, H. Mughrabi, Measurement of local elastic strains in aged monocrystalline nickel-base superalloys by cbed, Scr. Mater. 43 (2000) 859–864. https://doi.org/10.1016/S1359-6462(00)00498-X.

[32] W.C. Oliver, G.M. Pharr, An improved technique for determining hardness and elastic modulus using load and displacement sensing indentation experiments, J. Mater. Res. 7 (1992) 1564–1583. https://doi.org/10.1557/JMR.1992.1564.

[33] W.D. Nix, H. Gao, Indentation size effects in crystalline materials: A law for strain gradient plasticity, J. Mech. Phys. Solids 46 (1998) 411–425. https://doi.org/10.1016/S0022-5096(97)00086-0.

[34] V. Gerold, H.P. Karnthaler, On the origin of planar slip in f.c.c. alloys, Acta Metall. 37 (1989) 2177–2183. https://doi.org/10.1016/0001-6160(89)90143-0.

[35] B. Reppich, Some new aspects concerning particle hardening mechanisms in γ' precipitating Ni-base alloys—I. Theoretical concept, Acta Metall. 30 (1982) 87–94. https://doi.org/10.1016/0001-6160(82)90048-7.

[36] E. Nembach, K. Suzuki, M. Ichihara, S. Takeuchi, In situ deformation of the γ’ hardened superalloy Nimonic PE16 in high-voltage electron microscopes, Philos. Mag. A 51 (1985) 607–618. https://doi.org/10.1080/01418618508237581.

[37] E. Nembach, G. Neite, Precipitation hardening of Superalloys by ordered γ'-particles, Prog. Mater. Sci. 29 (1985) 177–319. https://doi.org/10.1016/0079-6425(85)90001-5.

[38] B. Reppich, P. Schepp, G. Wehner, Some new aspects concerning particle hardening mechanisms in γ' precipitating Ni-base alloys—II. Experiments, Acta Metall. 30 (1982) 95–104. https://doi.org/10.1016/0001-6160(82)90049-9.

[39] Y.-Z. Yin, Y. Lu, T.-P. Zhang, W.-Z. Han, Nanoindentation avalanches and dislocation structures in HfNbTiZr high entropy alloy, Scr. Mater. 227 (2023) 115312. https://doi.org/10.1016/j.scriptamat.2023.115312.

[40] I.A. Alhafez, O.R. Deluigi, D. Tramontina, N. Merkert, H.M. Urbassek, E.M. Bringa, Nanoindentation into a bcc high-entropy HfNbTaTiZr alloy—an atomistic study of the effect of short-range order, Sci. Rep. 14 (2024) 9112. https://doi.org/10.1038/s41598-024-59761-6.

[41] A.S. Argon, Strengthening mechanisms in crystal plasticity, Oxford university press, Oxford, 2008.

[42] R.C. Reed, The Superalloys: Fundamentals and Applications, Cambridge University Press, New York, 2006.

[43] B. Reppich, Particle Strengthening, in: R.W. Cahn, P. Haasen, E.J. Kramer (Eds.), Mater. Sci. Technol., 1st ed., Wiley, 2006. https://doi.org/10.1002/9783527603978.mst0054.

[44] W. Hüther, B. Reppich, Order hardening of MgO by large precipitated volume fractions of spinel particles, Mater. Sci. Eng. 39 (1979) 247–259. https://doi.org/10.1016/0025-5416(79)90063-6.

[45] R.W. Kozar, A. Suzuki, W.W. Milligan, J.J. Schirra, M.F. Savage, T.M. Pollock, Strengthening Mechanisms in Polycrystalline Multimodal Nickel-Base Superalloys, Metall. Mater. Trans. A 40 (2009) 1588–1603. https://doi.org/10.1007/s11661-009-9858-5.

[46] D. Tabor, The hardness of solids, Rev. Phys. Technol. 1 (1970) 145–179. https://doi.org/10.1088/0034-6683/1/3/I01.

[47] J.M. Rosenberg, H.R. Piehler, Calculation of the taylor factor and lattice rotations for bcc metals deforming by pencil glide, Metall. Trans. 2 (1971) 257–259. https://doi.org/10.1007/BF02662666.

[48] O.N. Senkov, J.-P. Couzinie, S.I. Rao, V. Soni, R. Banerjee, Temperature dependent deformation behavior and strengthening mechanisms in a low density refractory high entropy alloy Al10Nb15Ta5Ti30Zr40, Materialia 9 (2020) 100627. https://doi.org/10.1016/j.mtla.2020.100627.

[49] C.L. Fu, M.H. Yoo, Deformation behavior of B2 type aluminides: FeAl and NiAl, Acta Metall. Mater. 40 (1991) 703–711. https://doi.org/doi.org/10.1016/0956-7151(92)90012-4.

[50] Z. Sun, G. Song, J. Ilavsky, P.K. Liaw, Duplex Precipitates and Their Effects on the Room-temperature Fracture Behaviour of a NiAl-Strengthened Ferritic Alloy, Mater. Res. Lett. 3 (2015) 128–134. https://doi.org/10.1080/21663831.2015.1021492.

Supplementary Materials

Exploring room-temperature microplasticity in a B2-strengthened refractory compositionally complex alloy

Aparajita Pramanik[a], Chethan Konkati[a], Stephan Laube[b], Liu Yang[b], Sandipan Sen[b],
Alexander Kauffmann[b], Martin Heilmaier[b] and Ankur Chauhan[a*]

[a]Extreme Environments Materials Group (EEMG), Department of Materials Engineering, Indian Institute of Science (IISc), Bangalore, India, 560012

[b]Institute for Applied Materials (IAM-WK), Karlsruhe Institute of Technology (KIT), Engelbert-Arnold-Str. 4, 76131 Karlsruhe, Germany

[*]Corresponding author: ankurchauhan@iisc.ac.in

A. Microstructure and microhardness evolution at various heat-treatment conditions

Fig. S1 shows backscattered electron (BSE) micrographs acquired using a Helios NanoLab™ 650 scanning electron microscope (SEM) (Thermo Fisher Scientific Inc., Oregon, USA) equipped with a BSE detector. The microstructures of as-cast, as-homogenized, as-quenched (AQ), and samples aged at 900 °C for various durations are displayed. Additionally, Fig. S1 compares the microhardness of the AQ sample with those aged at 900 °C for different time intervals. Microhardness measurements were conducted with a 0.98 N applied load (HV0.1) using a Q10A+ Vickers hardness tester from Qness (Austria) in accordance with DIN EN ISO 6507 standards. The indents were manually positioned to avoid grain boundaries and pores. A minimum of 16 indents per sample were analyzed using the provided software. The BSE-SEM micrographs and microhardness data are sourced from [1].

The microhardness analysis indicates that aging leads to an increase in microhardness, peaking at 1 h, after which it declines, suggesting that the 1 h aging condition represents the peak-aged state. This is likely due to the B2 precipitates reaching their maximum volume fraction at the 1 h aged condition (see the corresponding BSE micrograph). After this point, there is a notable decrease in precipitate number density caused mainly by coarsening rather than growth. Therefore, it is inferred that the specimens aged for 1 h (peak-aged) and subsequently for 10 h, 100 h, and 1000 h exhibit comparable volume fractions of (0.15 ± 0.03) [1].

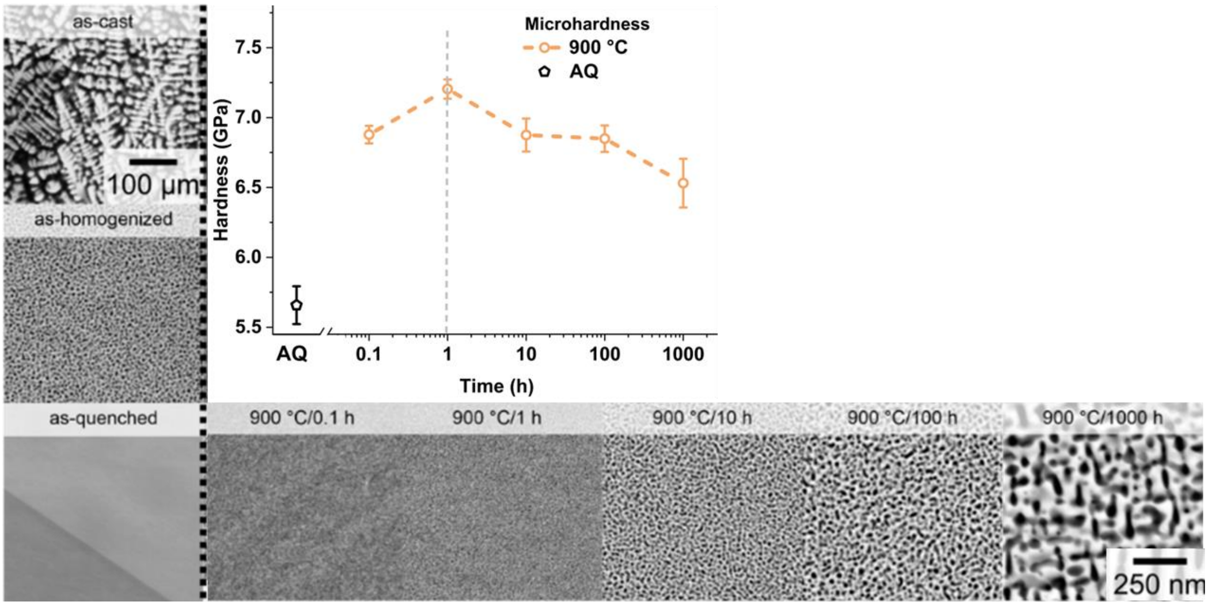

Fig. S1: BSE-SEM micrographs display the microstructures of as-cast, as-homogenized, and as-quenched (AQ) samples, as well as those aged at 900 °C for various durations. Additionally, a comparison of microhardness between the AQ sample and those aged at 900 °C for different time intervals is provided. Both the micrographs and hardness data are taken from [1].

B. Dislocations Burgers vector investigation

Fig. S2a displays a bright-field (BF) TEM micrograph of the deformed region beneath a nanoindent impression in the 900 °C 1h aged sample. The crack-free plastic zone shows a high density of dislocations, while the surrounding undeformed area remains dislocation-free. The region outlined with a dashed square in Fig. S2a, containing weakly coupled dislocations, was analyzed to determine their Burgers vector (b). Tilting this area (Fig. S2b) under different diffraction vectors (g) makes the dislocations invisible (Fig. S2c and S2d), allowing their Burgers vector to be identified as $\frac{1}{2}[11\bar{1}]$. Table S1 summarizes the g·b calculations supporting this result.

Table S1: The g·b table for determining the Burgers vector of dislocations in the alloy aged at 900 °C for 1 h.

Burgers vector	Zone axis (ZA)	[111]		[011]
(b)	g	$(10\bar{1})$	$(1\bar{1}0)$	$(2\bar{1}1)$
½[111]		0	0	1
½$[\bar{1}11]$		-1	-1	-1
½$[1\bar{1}1]$		0	1	2
½$[11\bar{1}]$		1	0	0

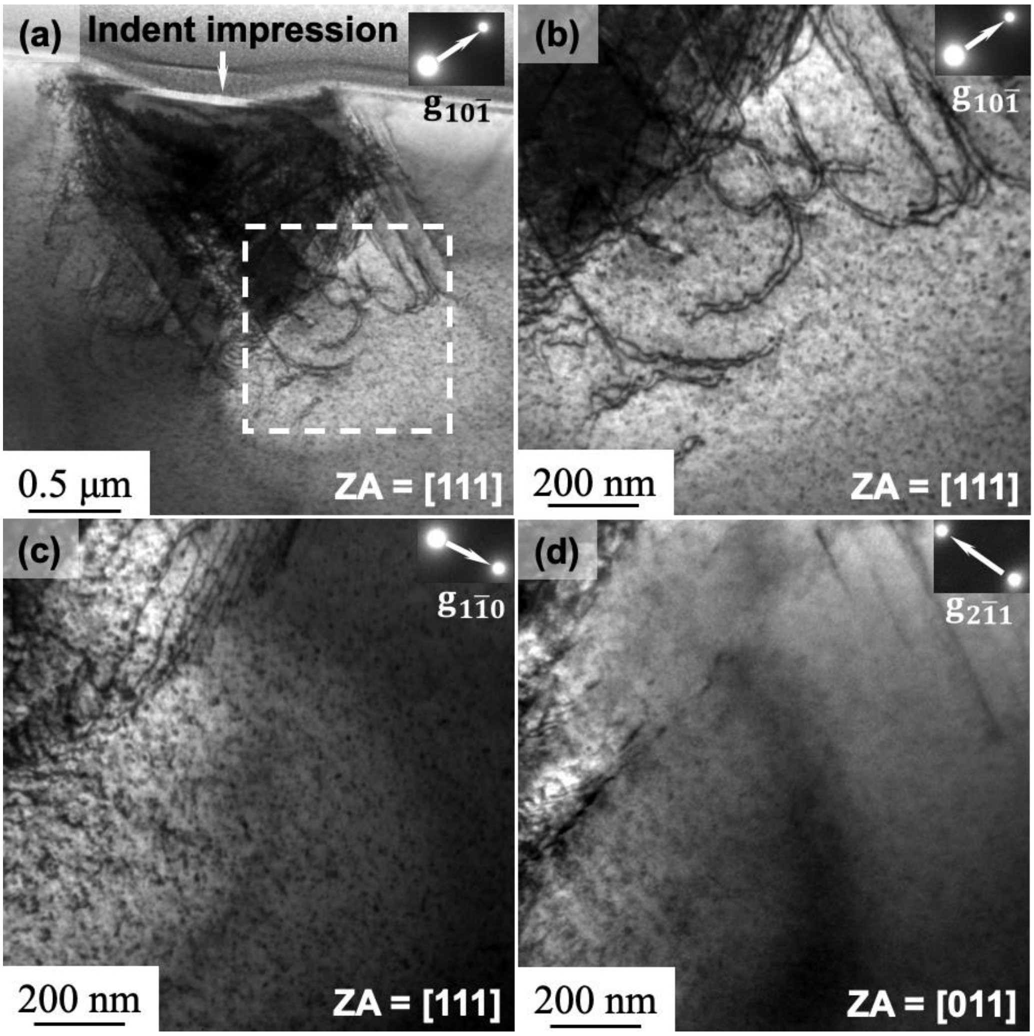

Fig. S2: BF-TEM micrographs illustrating deformation characteristics beneath an indent in the 27.3Ta–27.3Mo–27.3Ti–8Cr–10Al alloy aged at 900°C for 1 h. (a) Shows crack-free plastic zone shows a high density of dislocations, while the surrounding undeformed area remains dislocation-free. The square-marked area was analyzed using g·b analysis to determine the Burgers vectors of the dislocations. (b) A magnified view highlights weakly coupled dislocations, which become invisible in (c) and (d) under different two-beam conditions.

References

[1] S. Laube *et al.*, “Formation and thermal stability of two-phase microstructures in Al-containing refractory compositionally complex alloys,” *Sci. Technol. Adv. Mater.*, vol. 23, no. 1, pp. 692–706, Dec. 2022, doi: 10.1080/14686996.2022.2132118.